Thin film synthesis, structural analysis, and magnetic properties of novel ternary transition metal nitride MnCoN$_2$

Sita Dugu,[1,*] Rebecca W. Smaha ©,[1] Shaham Quadir,[1] Andrew Treglia ©,[2] Julia Martin,[1] Shaun O'Donnell ©,[1,2]
Sharad Mahatara,[1] Glenn Teeter ©,[1] Stephan Lany ©,[1] James R. Neilson ©,[2,3] and Sage R. Bauers ©[1,†]

[1]*Materials Sciences Center, National Renewable Energy Laboratory, 15013 Denver West Parkway, Golden, Colorado 80401, USA*
[2]*Department of Chemistry, Colorado State University, Fort Collins, Colorado 80523-1872, USA*
[3]*School of Advanced Materials Discovery, Colorado State University, Fort Collins, Colorado 80523-1872, USA*

Recent high-throughput computational searches have predicted many novel ternary nitride compounds providing new opportunities for materials discovery in underexplored phase spaces. Nevertheless, there are hardly any predictions and/or syntheses that incorporate only transition metals into new ternary nitrides. Here, we report on the synthesis, structure, and properties of MnCoN$_2$, a new ternary nitride material comprising only transition metals and N. We find that crystalline MnCoN$_2$ can be stabilized over its competing binaries, and over a tendency of this system to become amorphous, by controlling growth temperature within a narrow window slightly above ambient condition. We find that single-phase MnCoN$_2$ thin films form in a cation-disordered rocksalt crystal structure. X-ray photoelectron spectroscopy analysis suggests that MnCoN$_2$ is sensitive to oxygen through various oxides and hydroxides binding to cobalt on the surface. X-ray absorption spectroscopy is used to verify that Mn^{3+} and Co^{3+} cations exist in an octahedrally coordinated environment, which is distinct from a combination of CoN and MnN binaries and in agreement with the rocksalt-based crystal structure prediction. Magnetic measurements suggest that MnCoN$_2$ has a canted antiferromagnetic ground state below 10 K. We extract a Weiss temperature of $\theta = -49.7$ K, highlighting the antiferromagnetic correlations in MnCoN$_2$.

I. INTRODUCTION

Transition metal (TM) nitrides are important in several industrial applications, such as superconductors, hard coatings, plasmonics, photovoltaics, piezoelectrics, permanent magnets, and more [1–4]. Despite their known and promising functionality, TM nitride materials have been historically underexplored due to challenging synthesis routes and hurdles in achieving oxygen-free pure nitrides. To expand the number of known functional nitrides, several papers over the past decade have used high-throughput computations to identity nitride materials for various applications, including earth-abundant semiconductors, magnetic antiperovskites, and MAX phase precursors to MXenes [5–7]. The bounded nature of these works resulted in a few dozen nitride compounds to study, many of which were known. On the other hand, in 2019 Sun *et al.* [8] conducted a properties- and structure-agnostic

high-throughput computational search for ternary nitride compounds using a data-mined structure predictor [9] algorithm specifically trained for new nitride discovery. This search found 244 newly predicted stable ternary nitride phases, out of which 93 were in completely new chemical spaces (i.e., a pair of metals previously unknown to form a ternary nitride). Guided by these predictions, experimentalists have recently utilized radio frequency (rf) sputtering to synthesize several new ternary nitrides in the laboratory, such as MgTiN$_2$, MgHfN$_2$, Mg$_2$NbN$_3$ [10], MgZrN$_2$ [11], ZnTiN$_2$ [12], ZnZrN$_2$ [13], Zn$_2$SbN$_3$ [14], LaWN$_3$ [3], MnSnN$_2$ [15], Zn$_2$TaN$_3$ [16], and Zn$_2$VN$_3$ [17], to name a few.

While this is a fruitful materials discovery approach, none of these compounds contain only transition metals (TMs) [here, we consider Zn as chemically more like an alkaline earth (AE) main group element than a transition metal]. In fact, the 2019 paper [8] only found one new TM-TM-N chemical space containing a stable ternary nitride, Mn-Co-N. Figure 1(a) summarizes the new and known AE-TM-N and TM-TM-N as reported by this paper. Because many of the known TM-N binary compounds are useful compounds and magnetic materials, the predicted MnCoN$_2$ phase is a compelling materials discovery target. The structure predicted for MnCoN$_2$ in 2019 (entry mp-1029367 in the Materials Project) [18] is in a trigonal space group (sg, $R3m$) where the cations (Mn and Co) are bonded with anionic N to form MnN$_4$ and CoN$_4$ tetrahedra. Unlike the chalcopyrite structure, the predicted $R3m$ structure contains two inequivalent N^{3-} sites. On the first N^{3-} site, N^{3-} is bonded to one Mn cation and
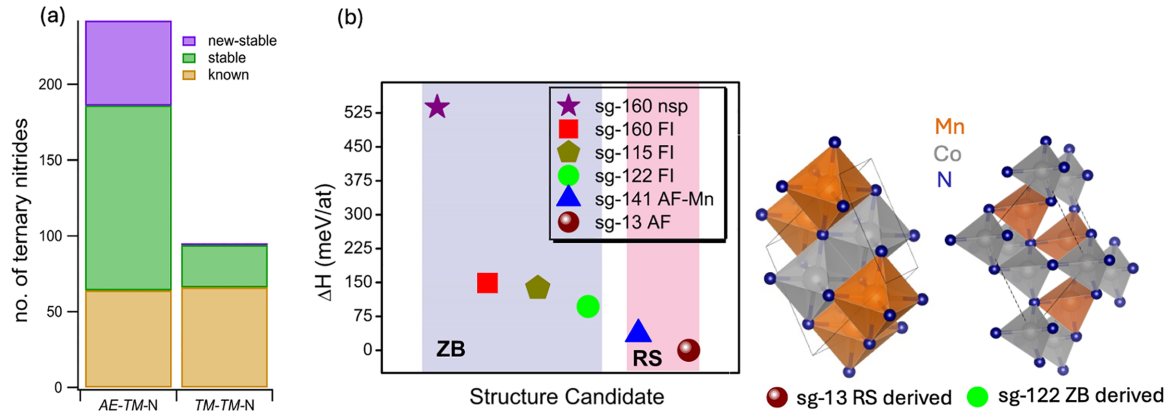

FIG. 1. (a) Bar chart of known, predicted metastable and new stable nitrides of alkaline earth–transition metal nitrides (AE-TM-N) and transition metal–transition metal nitrides (TM-TM-N). (b) Calculated enthalpies of five prototype structural candidates, sg-13 RS-derived and sg-122 ZB-derived crystal structure shown as the right side of (b).

three equivalent Co cations to form $NMnCo_3$ tetrahedra. In the second N^{3-} site, N^{3-} is bonded to one Co cation and three equivalent cations of Mn to form corner-sharing NMn_3Co tetrahedra.

It is important to contextualize $MnCoN_2$ among the competing MnN_x and CoN_x binary phases. While there are several in each system, we focus on those with a 1:1 metal:N ratio, like the $MnCoN_2$ compound of interest. We begin by discussing manganese nitrides. The manganese nitride with 1:1 cation:anion composition, θ-MnN, exists experimentally in a tetragonally distorted rocksalt (RS) structure (space group number 139) with antiferromagnetic (AFM) order with $T_N = 650$ K, measured from an exfoliated powder originally prepared by magnetron sputtering [19]. Conversely, some theories have proposed a cubic zinc-blende (ZB) structure under certain conditions [20,21]. Convex hull calculations from Li *et al.* [21]. predict a phase transition sequence for MnN with increasing pressure; first, the semiconducting nonmagnetic ZB phase transforms at 5 GPa to a metallic AFM phase in the NiAs structure, which at 40 GPa is destabilized versus a metallic ferromagnetic (FM) RS phase. Interestingly, while the low-pressure phases are not seen experimentally, on increasing pressure, Zheng *et al.* [22] recently observed a transition from AFM to FM order in rocksalt-derived MnN at 34 GPa. The transition to FM was associated with a reduction in cell volume of ca. 12% to 16 Å [3].

There are also several known nitrides of cobalt. While most of the early transition metal nitrides with a TM:N composition of 1:1 are reported as RS, this structure becomes destabilized with increasing electron count from populating antibonding orbitals [23]. Depending on the synthesis method, CoN had been reported as RS [24] and ZB [25]. Because both RS and ZB have underlying face-centered-cubic (fcc) lattice symmetry, the same family of x-ray diffraction (XRD) peaks are present in both. However, relative intensities in powder XRD patterns and peak positions both change between polymorphs. Suzuki *et al.* [26] synthesized ZB CoN by rf sputtering in 1995. In lieu of a full refinement, they showed that the material is ZB by comparing experimental XRD intensity with simulated patterns of CoN in both ZB and RS structures. They further observed that the ZB CoN exhibits Pauli paramagnetic properties, which was later theoretically

confirmed by Lukashev *et al.* [27] using spin-polarized calculations.

Considering the TM-N binaries, the unreported $MnCoN_2$ compound must be stabilized among multiple competing fcc structures, namely tetragonal RS MnN with octahedral coordination and cubic ZB CoN with tetrahedral coordination. Thus, the structure of $MnCoN_2$ might be either one of these or a mixture of both. In this work, we study this novel phase space and report the experimental synthesis of $MnCoN_2$, which adopts a cation-disordered rocksalt structure. We use laboratory and synchrotron XRD data, along with first-principles calculations, to explore the crystal structure, comparing the experimental data to the binary structures and the previously predicted structure. The octahedral environment is further supported by XAS experiments. We also show that $MnCoN_2$ exhibits canted AFM order at low temperature. Altogether, this work should motivate the identification and study of additional new TM_1-TM_2-N materials.

II. RESULTS AND DISCUSSION

A. Computational prediction

Since a high-throughput structure predictor approach does not always identify ground-state structures [8], and the existing $R3m$ $MnCoN_2$ entry in the Materials Project is non-spin-polarized (nsp), we begin by more thoroughly surveying candidate configurations for $MnCoN_2$. We selected five structural prototypes for $MnCoN_2$ and considered different possible magnetic configurations within a small eight-atom cell. The prototypes include three zinc-blende (ZB) -derived structures: the $MnCoN_2$ phase from the Materials Project (mp-1029367, sg-160), chalcopyrite ordered ZB (sg-122), and CuAu ordered ZB (sg-115), as well as two rocksalt (RS) -derived structures from our previous work on similar ternary nitrides: [10] α-NaFeO₂ ordered RS (sg-13) and γ-LiFeO₂ ordered RS (sg-141).

Figure 1(b) compares the total energy of the candidate crystal polymorphs in their most stable magnetic configuration. The lowest total energy was found for the α-NaFeO₂ RS-type structure in an AFM configuration [sg-13-AF; this is the zero reference energy in Fig. 1(b), and deviations from this energy are referred to as the polymorph energy difference].
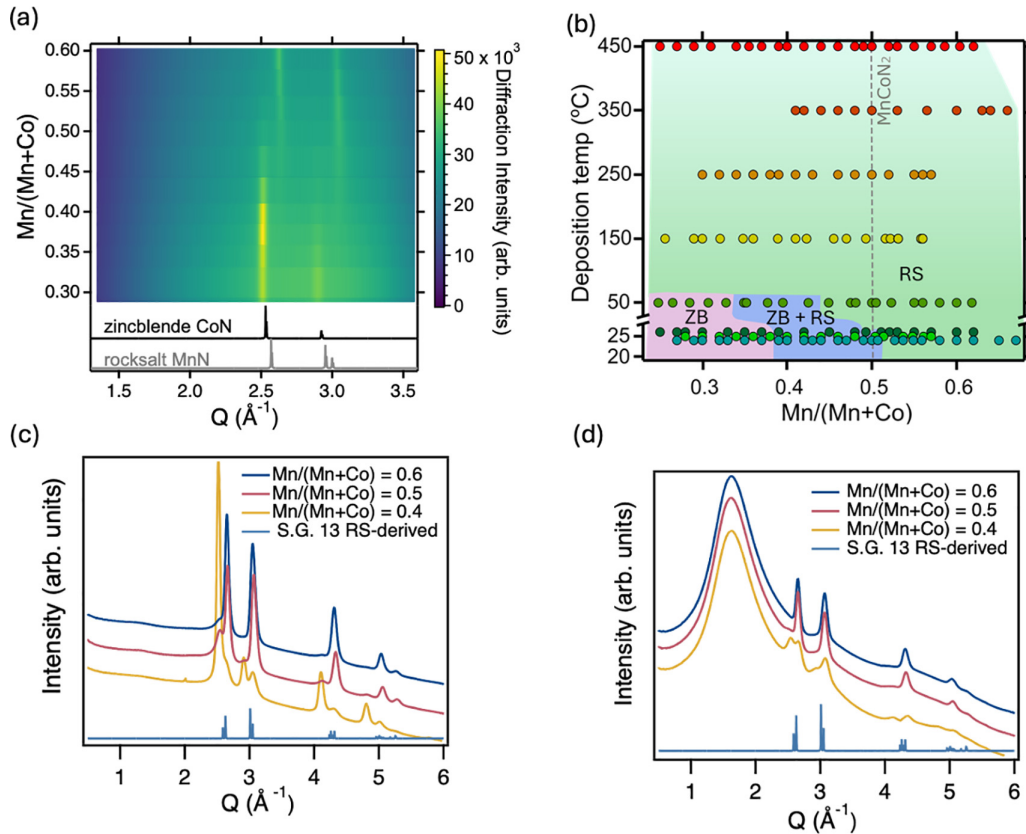
FIG. 2. (a) Laboratory XRD heatmap of a $MnCoN_2$ film grown at ambient conditions. Reference diffraction patterns of ZB CoN (black curve, ICSD entry no. 79936) and tetragonally distorted RS MnN (gray curve, ICSD entry no. 106932) are placed at the bottom. (b) Experimental phase map of $MnCoN_2$ deposited at various temperatures with all compositions measured by XRF. The shaded pink area indicates ZB phase while the green area represents RS phase. The blue shaded area represents the region where both RS and ZB regions are observed. The light green gradient with increasing temperature indicates lower crystallinity of the RS phase. Points with the same plot marker color were grown as part of the same combinatorial deposition. (c), (d) Synchrotron GIWAXS data measured from three different $Mn/(Mn + Co)$ compositions for films grown on (c) pSi and (d) EXG glass. Both films were grown in nominally ambient conditions. The calculated pattern in space group 13 is placed at the bottom.

Here, both the Mn and Co substructures have AFM order with local moments of $\sim 3.3 \mu_B$ and $\sim 2.5 \mu_B$, respectively. These moments suggest high-spin Mn^{4+} and Co^{2+} oxidation states. This AFM structure is 18 meV/atom lower in energy than the ferromagnetic (FM) configuration. We also tested ferrimagnetic (with Mn and Co having opposite spin direction) and low-spin Co configurations, which were found to be even less stable. The second most stable candidate, with a polymorph energy difference of $+36$ meV/atom, is the RS-derived structure based on the γ-$LiFeO_2$ prototype with AFM order (sg-141-AF-Mn) comprising high-spin Mn ($\sim 3.7 \mu_B$) and low-spin Co ($\sim 0.3 \mu_B$).

We find the most favorable ZB structure is ferrimagnetic chalcopyrite (sg-122-FI) at $+97$ meV/atom above the α-$NaFeO_2$ structure. Similarly, ZB-derived structures in sg-160 and sg-115 prefer ferrimagnetic configurations. Thus, the ZB-derived structures in Fig. 1(b) are calculated with ferrimagnetic ordering with Mn ($\sim 3.1-3.4 \mu_B$) and Co ($\sim 2.3-2.6 \mu_B$) spins in opposite directions. Also, there is a significant local moment of $\sim 0.3 \mu_B$ on nitrogen, suggesting partial reduction of N to N^{3-} and ambiguity in the oxidation states of Mn and Co. The nonmagnetic $MnCoN_2$ structure found in the materials project (sg-160-nsp) is energetically

very unstable at $+538$ meV/atom. Even in the ferrimagnetic state (sg-160-FI), it is still the least stable of the three ZB-derived structures at $+149$ meV/atom. Structure schematics of the lowest energy level RS-derived (sg-13) and ZB-derived (sg-122) phases are shown on the right side of Fig. 1(b).

The polymorph energy difference between sg-13 and sg-141 RS-derived structures is moderate at 36 meV/atom. While we did not explicitly sample cation-disordered structures computationally, because local order (i.e., Mn and Co configuration around a single N ion) changes between these prototypes, it is likely that entropy and/or kinetic hindrance during synthesis will result in experimental materials with cation disorder. Such disordered RS structures are well-known in both the high entropy ceramic [28] and the battery cathode [29] communities, and they have also been observed in other ternary nitrides [10]. This propensity for cation-disordered RS to form across so many chemistries was very recently shown to be statistical in nature [30].

B. $MnCoN_2$ synthesis

Figure 2(a) displays 44 laboratory XRD patterns collected as a function of position on a compositionally graded

Mn-Co-N film on a Si substrate. The diffraction intensity is presented as a heatmap against the measured cation composition and scattering vector, Q ($\lambda = 1.54059$ Å). The film was grown without active heating, which we refer to as "ambient" in this article. The traces on the bottom of the plot are simulated XRD patterns; the black curve is the reference pattern for ZB CoN [26], whereas the gray curve is that of tetragonally distorted RS MnN [19]. Depending on the composition, the experimental patterns resemble the reference patterns: ZB at higher Co concentrations, RS at higher Mn content, and both sets of peaks around Mn/(Mn + Co) = 0.5. For a given chemical system, peaks from (tetrahedrally coordinated) ZB are shifted to lower Q than (octahedrally coordinated) RS because, while both are fcc, ZB is a lower density structure with a larger unit cell. Thus, the abrupt shift in peak position suggests that the local coordination changes with an overall trend in $Mn_{1+x}Co_{1-x}N_2$ of ZB when Co-rich, RS when Mn-rich, and coexistence around the stoichiometric condition. While further experiments would be needed to assess local composition, our observation suggests that it might be possible to realize stoichiometric $MnCoN_2$ in either ZB or RS structures. Within each set of peaks (i.e., ZB or RS), a subtle shift in Q is observed with composition, suggesting that, at least for small magnitudes of x in $Mn_{1+x}Co_{1-x}N_2$, Co is incorporated into RS and Mn into ZB, as opposed to distinct MnN and CoN binary phases. The lack of additional XRD peaks beyond those in basic ZB/RS patterns is an indication of significant disorder on the cation sublattice of the ternary phase(s).

Similar behavior is seen with active heating to a deposition temperature (T_d) of 50 °C, but the RS region shifts to lower Mn compositions, even beyond the stoichiometric condition. Thus, at slightly elevated temperatures, the stoichiometric single-phase cation-disordered RS compound $MnCoN_2$ can form. Samples grown at 150 °C exhibit a single phase for all Mn concentrations studied, as shown in Fig. S1a of the Supplemental Material [31]. Despite observation of a single RS phase at high T_d, the overall crystallinity of the film is lower as indicated by diffraction peaks with large full width at half-maximum (FWHM), a trend that increases with higher deposition temperatures. The FWHM of the (111) and (200) peaks for T_d of ambient, 50 °C, and 150 °C are shown in Fig. S1b.

Films grown at several conditions are summarized on a phase diagram as a function of deposition temperature (T_d) and composition in Fig. 2(b), where each point color represents a different compositionally graded film. Films grown at 150 °C and above only show a RS phase regardless of Mn/(Mn + Co) values. However, the crystallinity of the samples progressively decreases with an increase in deposition temperature, highlighted by the color gradient area in Fig. 2(b). For samples deposited at ambient and up to 50 °C, the observed phases (ZB and RS in our system) depend on the Mn/(Mn + Co) values. For films grown at 50 °C, the ZB phase is observed when Mn/(Mn + Co) < 0.34 and RS is observed when Mn/(Mn + Co) > 0.45; both phases appear in the range 0.34 ⩽ Mn/(Mn + Co) ⩽ 0.45. At ambient, these stability windows are moved to higher Mn content; the ZB phase is seen when Mn/(Mn + Co) < 0.38 and the RS phase when Mn/(Mn + Co) > 0.52, with mixed ZB and RS at intermediate compositions. Multiple growths with similar

parameters are performed to check the phase stability when Mn/(Mn + Co) = 0.5. It appears that the Mn/(Mn + Co) = 0.5 composition is on the cusp of a phase change. At this composition, we observed only RS phase for one growth. However, on subsequent, nominally identical growths, both RS and ZB phases are present. XRD patterns from these films, and others deposited at various temperature (ambient to 350 °C), are shown in Fig. S1c. This difficulty controlling the $MnCoN_2$ phase might be expected to lead to property variations in follow-on studies of the material.

To further diagnose the crystallinity of samples, we characterized them with synchrotron grazing incidence wide-angle x-ray scattering (GIWAXS; $\lambda = 0.97625$ Å). Figure 2(c) shows integrated GIWAXS patterns of films grown at ambient with Mn/(Mn + Co) = 0.4, 0.5, and 0.6. For the compositions Mn/(Mn + Co) = 0.5 and 0.4, peak splitting indicative of RS/ZB coexistence is observed; Mn/(Mn + Co) = 0.6 is closest to phase pure. To understand the role of thermal conductance of the substrate on phase formation, films were subsequently also grown on borosilicate glass (Corning Eagle XG glass, EXG) at ambient conditions. Despite the lack of active heating, both the lower thermal conductivity (< $1 \, \mathrm{W \, m^{-1} \, K^{-1}}$ for glass versus > $100 \, \mathrm{W \, m^{-1} \, K^{-1}}$ for Si) and the thicker substrate (1.1 mm for glass versus 0.6 mm for Si), coupled with front-side heating from the plasma, result in an elevated growth temperature during deposition on glass. GIWAXS patterns from the same Mn/(Mn + Co) = 0.4, 0.5, and 0.6 compositions but grown on glass substrates are shown in Fig. 2(d). With the slightly elevated T_d afforded by deposition onto the glass substrate, the RS phase is observed for Mn/(Mn + Co) = 0.5 and 0.6; only at high Co content (low Mn content) is a mixed phase observed. The detector images of films grown on Si substrate and EXG are shown in Fig. S2.

To summarize Fig. 2, the apparent phase instability from minor thermal differences created by the plasma environment or different substrates during ambient temperature deposition suggests the growth process is highly sensitive to the thermal environment. At the same time, deposition temperatures ⩾150 °C reduce crystallinity. One explanation for this could be N loss at elevated T_d; $MnCoN_2$ lacks an electropositive metal that helps stabilize N-rich nitrides [8], and instead contains only transition metals well known to accommodate substoichiometric N [32]. For films grown just above ambient (i.e., at 50 °C), the metal-stoichiometric films are highly crystalline and reliably form in the RS structure.

C. Chemistry of Mn and Co in $MnCoN_2$

X-ray photoelectron spectroscopy (XPS) is a powerful tool to understand the electronic and surface chemical environment of a system. XPS was conducted at three to four points with varying Mn:Co concentration for films grown at 50 and 150 °C on a Si substrate. Figures 3(a)–3(d) show the Mn 2p, Co 2p, N 1s, O 1s spectra acquired from the $MnCoN_2$ film grown at 50 °C. The Co and Mn 2p orbitals [Figs. 3(a) and 3(c)] each display characteristic spin-orbit splitting (2$p_{3/2}$ versus 2$p_{1/2}$). Both the Mn 2p and N 1s spectra [Figs. 3(a) and 3(b)] can be fit with asymmetric peaks consistent with a single chemical state for each element. In the Co 2p core level, the two main peaks at 780 and 795.4 eV correspond to Co 2$p_{3/2}$
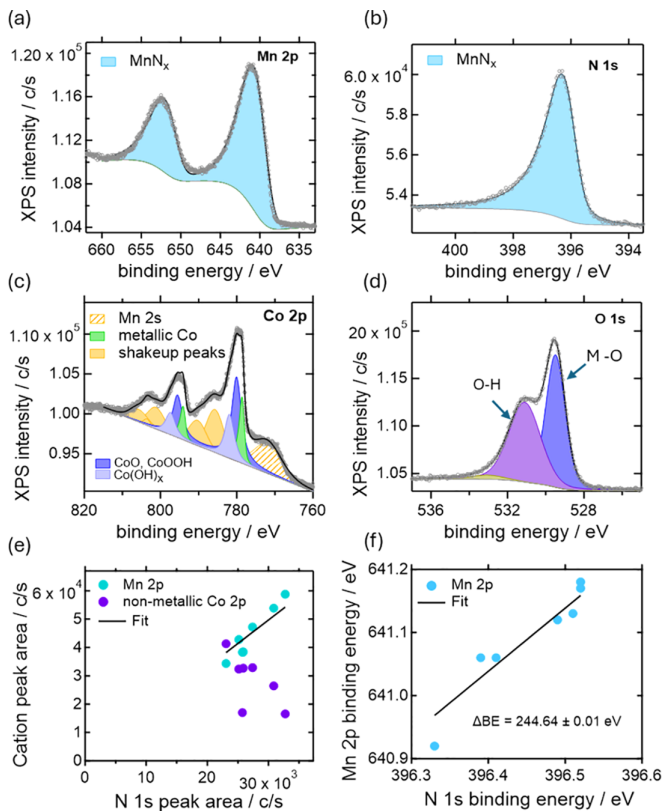
FIG. 3. Surface XPS spectra of $MnCoN_2$. Panels (a)–(d) are XPS spectra of Mn $2p$, N $1s$, Co $2p$, and O $1s$ of stoichiometric $MnCoN_2$ grown at 50 °C. (e) The cation peak area vs N $1s$ peak area for compositional variation $0.35 < Mn/(Mn + Co) < 0.58$. (f) Binding energy of Mn $2p$ vs N $1s$ for compositional variation $0.35 < Mn/(Mn + Co) < 0.58$, with a linear fit.

and Co $2p_{1/2}$ respectively [33,34]. The core levels [Fig. 3(c)] require peaks corresponding to at least three distinct chemical states, with the presence of additional shakeup peaks and a contribution from the Mn $2s$ orbitals. The dark blue (780.15 and 795.55 eV) and light blue (782.2 and 797.4 eV) peaks are tentatively associated with Co oxides and hydroxides [35,36]. The presence of hydroxides is further supported by the appearance of several shakeup peaks that are often associated with the adsorption of surface oxides/hydroxides, observed at 785.9, 801.4, 790.5, and 805.8 eV [36,37]. The peak at 771.8 eV is attributed to Mn $2s$, while the peaks at 778.6 and 794.15 eV are assigned to metallic Co. Collectively, these results indicate that Co–O bonds form preferentially in the near-surface region of $MnCoN_2$ during air exposure, leading to decomposition into Co-(O,OH) and Mn-N phases.

XPS indicates the presence of large amounts of oxygen in the near-surface region, which is also seen in the bulk of a film by Rutherford backscattering spectrometry (RBS), shown in Fig. S3. This suggests the presence of surface oxides, not unexpected for nitrides exposed to atmosphere [37]. O $1s$ spectra [Fig. 3(d)] can be subdivided into two peaks at 531.2 and 529.5 eV. The blue-shaded O $1s$ feature centered at 529.5 eV is due to lattice O^{2-}, and the position is consistent with that expected for metal oxide(s) [38,39]. The higher binding energy O $1s$ (purple shaded) feature at 531 eV

likely corresponds to the surface hydroxyls, under coordinated lattice oxygen [40], and/or traces of oxidized contaminants [39,41]. A small yellow shaded peak featured at higher binding energy (533.2 eV) is attributed to carbon contamination.

Similar XPS spectra, shown in Fig. S4 (a)–(d), were collected at multiple compositions in the range $0.4 < Mn/(Mn + Co) < 0.6$, for deposition temperatures of 50 and 150 °C. The integrated intensities of the Mn, Co, and N peaks discussed above are plotted against each other in Fig. 3(e). This plot shows a strong linear correlation between the Mn $2p$ and N $1s$ peak areas, indicating that these constituents very likely participate in the same phase. Further evidence for the existence of an Mn-N phase is the linear correlation (with slope = 1) between binding energies for the Mn $2p$ and N $1s$ peak, shown in Fig. 3(f). At the same time, the sum of nonmetallic Co $2p$ peak areas is anticorrelated with the N $1s$ peak area, suggesting that there are no phases present that involve both Co and N. Based on all of these observations, we assign the Mn $2p$ and N $1s$ peaks to a MnN_x phase, as annotated in Figs. 3(a) and 3(b), with a Mn:N ratio ∼1.7 based on the observed sensitivity-factor corrected peak areas. The $\Delta BE = 244.64 \pm 0.01$ eV value represents the characteristic binding energy separation between the N $1s$ and Mn $2p$ peaks for the MnN_x phase. On the other hand, the nonmetallic Co $2p$ peaks appear anticorrelated to N $1s$. In fact, the total peak area of Co $2p$ (Co oxides and hydroxides) has a positive correlation with M–O, whereas Mn does not, as shown in Fig. S5. This analysis indicates that Mn–N bonds are likely stronger and better resist replacement of N with O compared to Co–N bonds on the surface of $MnCoN_2$, and that the nitrogen detected is associated with Mn. An implication of the higher affinity for Co to bond to O over Mn is that more Co is involved in secondary phases. This suggests that an excess of Co [as measured by a global composition probe such as x-ray fluorescence (XRF)] will be needed to achieve locally stoichiometric $MnCoN_2$ in thin films containing several percent of O.

Chemical information of the films was further studied using x-ray absorption spectroscopy (XAS) to understand the bulk chemistry of the system. Three compositions with $Mn/(Mn + Co) = 0.6$, 0.5, and 0.4 for films grown at ambient, 50 °C, and 150 °C were selected and analyzed for x-ray absorption near-edge structure (XANES) spectroscopy and extended x-ray absorption fine structure (EXAFS) spectroscopy at both the Mn and Co K-edges. The Mn K-edge XANES of films grown at ambient for an $Mn/(Mn + Co)$ value of 0.6, 0.5, and 0.4 is presented in Fig. 4(a), along with references MnO and Mn_2O_3 for comparison. The absorption edges (E_o) for all three $Mn/(Mn + Co)$ compositions are in the range 6547–6547.9 eV, which is close to that of Mn_2O_3, hence the oxidation state can be attributed to Mn^{3+} [42–45], as shown in Fig. 4(a). The slight shift to lower photon energy from the Mn_2O_3 standard is expected as N anions are less electron withdrawing, even for the same nominal +3 oxidation state.

Co K-edge XANES spectra of samples grown at ambient are shown along with the standards CoO and $LiCoO_2$ in Fig. 4(b). All Co K-edge XANES spectra of the Mn–Co–N films show a preedge feature at ∼7710 eV; the primary edge measured lies between the absorption edges of CoO and $LiCoO_2$, suggesting
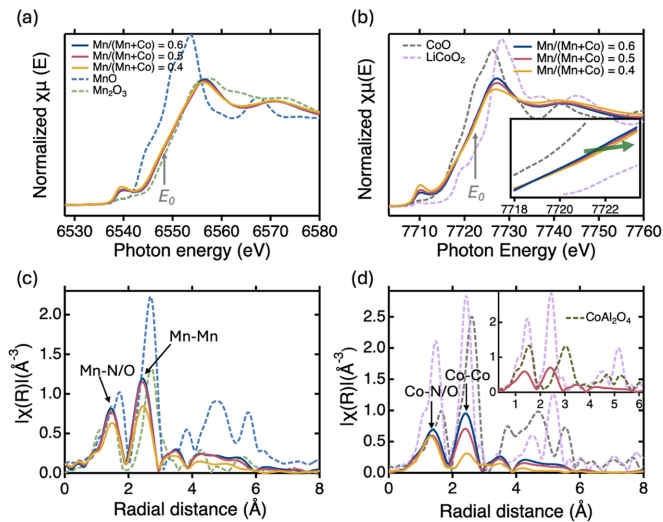
FIG. 4. XAS data of films with $Mn/(Mn + Co) = 0.6, 0.5, 0.4$. Panels (a) and (b) are XANES data at the Mn and Co K-edges. The inset of panel (b) shows the energy shift of the absorption edge on increasing Co content. Panels (c) and (d) are EXAFS data at the Mn and Co K-edges.

an oxidation state for Co between $+2$ and $+3$ [46]. On increasing Co content, the absorption edge is progressively shifted to positive energy as shown by the arrow in the inset of Fig. 4(b). This suggests there is more positive charge density around Co (i.e., a greater degree of electron withdrawal) at high Co concentrations [37]. Some oxygen is seen through the bulk of slightly Co-rich films in RBS, as discussed in section 2 of the Supplemental Material (Figs. S3a,b). This is common in sputtered nitride materials during the discovery stages of research, to the point where they are sometimes considered N-rich oxynitrides, but nearly O-free variants can often be achieved after continued optimization using specialized growth techniques [3,11,47]. Because the bulk oxygen concentration is set by the background pressure of oxygen-containing species during growth, and oxygen clearly prefers to bind to Co over Mn in $MnCoN_2$, we posit that a few extra percent of Co is needed to locally achieve stoichiometric $MnCoN_2$ among some CoO that is also formed. Whether the intermediate $2+/3+$ character of Co is indicative of an intermediate oxidation state of Co in $MnCoN_2$ or mixed Co oxidation states (which might be expected in, for example, $MnCoN_2$ + amorphous CoO) is at this point unknown.

Figure 4(c) shows Fourier-transformed EXAFS spectra $[|\chi(R)|]$ at the Mn K-edge for the films with $Mn/(Mn + Co) = 0.6, 0.5$, and 0.4. For all films (shown in S5), the intensity of both the first and second shells decreases with higher Co composition, and there is no change in the shell expansion or contraction in the first and second shell, indicating the absence of structural (crystal) changes [48]. $|\chi(R)|$ results from the Co K-edge for the same $Mn/(Mn + Co) = 0.6, 0.5$, 0.4 positions are shown in Fig. 4(d). EXAFS pair distance data have previously been used to compare relative fractions of metals in octahedral and tetrahedral sites in Mn- and Co-containing spinel oxides [49]. Because of the similar ionic size between Mn and Co [50], peaks arise around the same

places in Mn and Co radial distribution functions for a given coordination environment. For the spinel oxides, intensity at a radial distance (r) of 2.5 Å was attributed to octahedral Mn and Co, and intensity at $r = 3.0$ Å was attributed to tetrahedral Mn and Co [49]. Here, we see high intensity at $r = 2.3$ Å for Mn- and Co-edge radial distribution functions, suggesting that both Mn and Co in $MnCoN_2$ are octahedral. The peak shift to lower r relative to the oxide spinel is expected because the metal-anion bond lengths from octahedrally coordinated nitride binaries are slightly smaller than in the corresponding oxides. The inset of Fig. 4(d) compares the Co K-edge EXAFS signal of $MnCoN_2$ to standards where the Co is in both octahedral ($LiCoO_2$ in the purple dashed curve) and tetrahedral ($CoAl_2O_4$ in the orange dashed curve) environments. The film's curve is a much closer match with the octahedrally coordinated $LiCoO_2$ standard. Altogether, these EXAFS data provide strong evidence beyond XRD that ternary $MnCoN_2$ is distinct from the combination of RS MnN and ZB CoN binary phases.

Octahedral Mn^{3+} is Jahn-Teller active, but we did not see any indication of distortions or symmetry lowering (via peak splitting) in XRD or GIWAXS. One explanation could be that cation disorder prevents a cooperative distortion. In this case, local distortions may still be observed as low-r peak-splitting in EXAFS. We do not identify any perceivable peak splitting in the $MnCoN_2$ EXAFS data, but splitting is also not present in the EXAFS data for the Mn_2O_3 standard, which is also octahedral (bixbyite) Mn^{3+}. Because of this, we cannot rule out Jahn-Teller activity in $MnCoN_2$.

The XANES and EXAFS of the films grown at $150\,°C$, $50\,°C$, and ambient are presented in Fig. S6a-d. There is a consistent ordering of absorption edges for Mn and Co in XANES (Figs. S6a and S6b). The XANES data of all films show a well-defined preedge feature indicating a noncentrosymmetric structure [51]. The feature is more pronounced in Co-rich compositions, where a tetrahedral environment is more likely. Since there is no indication of a crystalline noncentrosymmetric structure in XRD, this feature could be due to local-tetrahedral motifs in amorphous regions or at grain boundaries. The shift in preedge peak position in Mn K-edge is smaller than in the Co K-edge, indicating the change in oxidation state in Mn is smaller than in Co, in agreement with XPS analysis and from EXAFS curves. Mn K-edge EXAFS (Fig. S6c) shows a slightly lower magnitude for $Mn/(Mn + Co) = 0.4$ for films grown at all T_d. The consistency of Mn–N and Mn–Mn bonding in Mn EXAFS confirms that the system is stable [37] at $150\,°C > T_d >$ ambient for $0.6 > Mn/(Mn + Co) > 0.4$. On other hand, in Co K-edge EXAFS (Fig. S6d), the Co–Co bond intensity is lower for higher Co content (lowest for the sample grown at $150\,°C$). This indicates that Co tends to oxidize at higher concentrations, consistent with the XPS results.

D. Magnetic properties

From XPS and XAS analyses, we conclude that both Mn^{3+} and Co^{3+} cations reside in octahedral coordination environments, with the presence of some Co^{2+} that is possibly localized around O impurities. With octahedral Mn^{3+}, one expects four unpaired electrons in the high-spin configuration
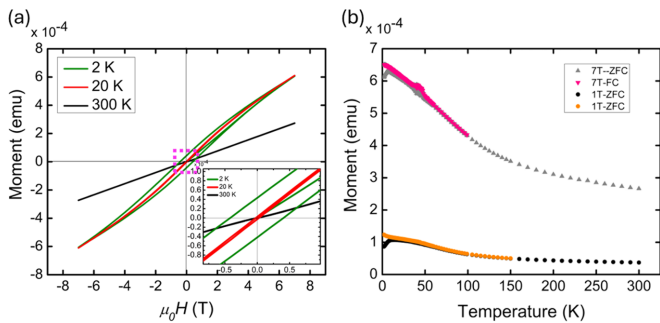
FIG. 5. Magnetic properties of a film with $Mn/(Mn + Co) = 0.5$ grown at $50\,°C$. (a) Moment of the $MnCoN_2$ film as a function of applied field measured at 2, 20, and 300 K. Inset is the magnified graph at lower field range. (b) Zero-field-cooled (ZFC) and field-cooled (FC) moment as a function of temperature measured at 1 and 7 T. Note: The FC scan was stopped once the measurement reached an identical value as the ZFC data.

($\mu_{\text{eff}} = 4.9\,\mu_B$) and two unpaired in the low-spin configuration ($\mu_{\text{eff}} = 2.8\,\mu_B$). For Co^{3+}, one expects an $S = 0$ diamagnetic low-spin configuration, whereas high-spin would have four unpaired electrons ($\mu_{\text{eff}} = 4.9\,\mu_B$). With Co^{2+}, one expects three unpaired electrons with some unquenched orbital momentum with high spin ($\mu_{\text{eff}} = 5.2\,\mu_B$).

DC magnetization was measured for a film with $Mn/(Mn + Co) = 0.5$ grown at $50\,°C$. Figure 5(a) shows the magnetization as a function of applied magnetic field, measured at temperatures ranging from 2 to 300 K. Data are plotted after subtracting the substrate's background signal, which was measured on a comparable piece of Si. Hysteresis is observed at 2 K, and it disappears at $T = 20$ K, suggesting that a magnetic transition exists at $T < 20$ K. At 2 K, the coercive field (H_c) of the film is observed to be 0.4 T, and there is a small net moment, as illustrated by the inset in Fig. 5(a).

Temperature-dependent measurements were performed under field-cooled (FC) and zero-field-cooled (ZFC) conditions, at 1 and 7 T. At both fields, cusps appear at 10 K [Fig. 5(b)]. A small bifurcation between the ZFC and FC data, and the absence of a significant shift in the ZFC peak position over a wide field range (1–7 T), suggests a potential AFM transition at 10 K and the presence of some disorder. However, because we observed a small hysteresis at 2 K, we hypothesize that the ground state is likely canted AFM or ferrimagnetic order below 10 K.

We also note a change in slope in the inverse magnetization at high temperature, visible in both Fig. 5(b) and a plot of H/moment versus temperature (Fig. S7a). From these data, we hypothesize that the most likely scenario is that $MnCoN_2$ is fully paramagnetic at high temperature, and short-range AFM correlations start to disrupt ideal paramagnetic behavior below ~ 150 K. We observed linear behavior of the moment at high temperature in a plot of the inverse moment (Fig. S7b), which is consistent with paramagnetic behavior, and therefore we performed a Curie-Weiss fit from 170 to 300 K. While this fit cannot yield a meaningful Curie constant as we do not know the film mass precisely enough to calculate susceptibility, a meaningful Weiss temperature can still be extracted. The Weiss temperature (Θ) resulting from this fit is $-49.7(3)$ K, supporting the assignment of AFM interactions in $MnCoN_2$.

The canted AFM ordering temperature of ~ 10 K is much lower than that of the reported binary Mn nitrides (Mn_4N at 745 K [52], Mn_3N_2 at 920 K [53], and $MnN_{1-\delta}$ at 650 K [19]) and FM ordering of binary Co nitrides (Co_3N at 615 K and $Co_{2.8}N$ at 450 K [54]). This makes our observation of a low-temperature order in $MnCoN_2$ surprising. However, cation disorder was recently found to suppress magnetic order in $MnSnN_2$ in a wurtzite-derived structure [15], lending credibility to our hypothesis of low-temperature canted AFM order. In rocksalt $MnCoN_2$, the presence of cation disorder between diamagnetic low-spin Co^{3+} and magnetic Mn^{3+} would imply weak interactions, for example through magnetic dipoles, or perhaps puddles of order that do not encompass the entire sample. Further work will be required to probe the level of cation disorder in this material and explore its effect on properties. On other hand, we see evidence of CoO_x phases through chemical analysis, and Co_3O_4 shows magnetic ordering below 20 K [55]. However, XRD does not indicate the presence of crystalline Co_3O_4 oxides, so we conclude the magnetic properties observed here are likely dominated by the $MnCoN_2$ phase. Another possible scenario for $MnCoN_2$ could be that it is AFM at all temperatures measured here like the binary Mn nitrides, although we were not able to probe this hypothesis directly in this work; the bifurcation between FC and ZFC, shown in Fig. 5(b), and opening of the hysteresis loop below ~ 20 K [Fig. 5(a), inset], would then occur from spin canting and pinned domains that require reorientation.

III. CONCLUSION

A new ternary nitride material $MnCoN_2$ has been discovered in thin film form. The compound was initially predicted in a trigonal $R3m$ space group with Mn and Co tetrahedrally bonded with four N atoms, but our calculations suggest the material is more stable in a rocksalt-derived structure with octahedral coordination environments. Our experimental syntheses performed on different substrates confirm that $MnCoN_2$ films exhibit a cation-disordered rocksalt phase and that the deposition temperature must be carefully controlled to achieve single-phase, highly crystalline material. XPS suggests that oxygen preferentially bonds to Co on the surface of $MnCoN_2$. Further experiments using x-ray absorption spectroscopy verify octahedral coordination of Co^{3+} and Mn^{3+} in the bulk of the film, confirming the rocksalt phase in this system. Magnetic studies show that the system possesses canted AFM order with a transition at ~ 10 K and a small net moment. In the future, the study of magnetic properties with improved film quality and under controlled cation antisite populations would be interesting. Our experimental confirmation of this new TM_1-TM_2-N material adds one more compound to the library of ternary nitrides, motivating renewed effort in predicting and discovering new materials in similar ternary spaces.

IV. METHODS

A. Synthesis

Combinatorial $MnCoN_2$ thin films were deposited using an RF magnetron sputtering system at several temperature ranges of $25-450\,°C$. The thin films were deposited by cosputtering

3″ Co (99.98%) and 3″ Mn (99.99%) targets (Kurt J. Lesker Co.) placed at a 120° angle to each other, thus creating a gradient in cation fluxes resulting in compositional gradient deposition of $MnCoN_2$. Most films were grown for 2 h, resulting in thicknesses ranging from about 400 to 700 nm. Samples for XAS studies were grown for 10 min, resulting in correspondingly thinner films, but possibly higher overall oxygen concentrations from surface oxidation. Prior to deposition, the chamber was evacuated to a base pressure of $\sim 3 \times 10^{-7}$ Torr. All films were grown at a working pressure of 4 mTorr, provided by 20 sccm Ar and 5 sccm of molecular N_2. No additional nitrogen activation was employed. Most of the films were deposited on 50.8 cm × 50.8 cm pSi (100) wafers with a native oxide layer (~ 2 nm), while some were deposited on 12.7 cm × 1 cm glassy carbon (HGW GmbH, Germany) and on Corning Eagle XG glass (EXG, electronically insulating and optically transparent, with a silicon back plate to transfer heat during deposition) for certain property measurements as mentioned in the text. All samples were cleaned with isopropanol and DI water followed by N_2 gas blow before loading into the chamber. The targets were presputtered for at least 30 min with the shutter closed to remove surface oxide.

B. Characterization

Experimental data for this study have been analyzed using the COMBIgor package [56], and they are available publicly in the National Renewable Energy Laboratory (NREL) high-throughput experimental material database [57,58]. Thin films grown on 2″ × 2″ substrates were mapped as 4 × 11 points, called "libraries." A Bruker D8 x-ray diffractometer using θ-2θ geometry and Cu $K\alpha$ radiation and equipped with an area detector was used to map the libraries. High-resolution synchrotron grazing incidence wide angle x-ray scattering (GIWAXS) measurements were performed on select samples at beamline 11–3 at the Stanford Synchrotron Radiation Lightsource, SLAC National Accelerator Laboratory. The data were collected with a Rayonix 225 area detector at room temperature using a wavelength of $\lambda = 0.976\,25$ Å, a 1° or 3° incident angle, a 150 mm sample to detector distance, and a beam size of 50 μm vertical × 150 μm horizonal. Cation compositions were measured with a Fischer XDV-SDD x-ray fluorescence instrument with an Rh source and a 3-mm-diam spot size. The measurements were performed at ambient temperature and pressure with an exposure time of 120–180 s for each measurement. Rutherford backscattering spectrometry (RBS) was used to further check the cation and anion concentration. RBS was run in a 168° backscattering configuration using a model 3S-MR10 RBS system from National Electrostatics Corporation with a 2 MeV He$^+$ beam energy. Samples were measured for a total integrated charge of 160 μC. RBS spectra were modeled with the RUPM software package [59].

XPS measurements were performed in a Physical Electronics VersaProbe III instrument using monochromatic Al-$K\alpha$ x-rays ($h\nu = 1486.7$ eV). High-resolution XPS spectra were acquired at a 55 eV pass energy, and the binding-energy scale was calibrated using the Au $4f_{7/2}$ (83.96 eV) and Cu $2p_{3/2}$ (932.62 eV) core levels and the Fermi edge ($E_F = 0.00$ eV) measured on sputter-cleaned metal foils. Curve-fitting of XPS spectra was performed and fitted in Igor Pro.

X-ray absorption spectroscopy (XAS) was performed at beamline 6-BM at the National Synchrotron Light Source (NSLS-II) at Brookhaven National Laboratory. The beamline was equipped with a paraboloid collimating mirror coated with rhodium, a monochromator utilizing (111) crystal, and a flat mirror designed for rejecting harmonic frequencies. The films on which XAS measurements were carried out were grown on glass substrates to mitigate the issue of Bragg diffraction from the crystalline substrate. Spectra of films were collected at room temperature in fluorescence mode, whereas the spectroscopic references, including CoO powder (99.5%, Sigma Aldrich), MnO powder (99.5%, Sigma Aldrich), Mn_2O_3 (99.9%, Sigma Aldrich), $LiCoO_2$ (99.5, Sigma Aldrich), and $CoAl_2O_4$ (99.5, Sigma Aldrich), were measured in transmission mode. Six scans for the Co K-edge and three scans for the Mn K-edge were collected and averaged to further improve the signal-to-noise ratio of the absorption spectra. Fourier-transformed EXAFS spectra were processed with a k^3-weighting Hanning window (3–9.9 Å) and without phase correction. Data were analyzed in Athena within the Demeter software suite [60].

Magnetic properties were measured via superconducting quantum interference device (SQUID) magnetometry in a Quantum Design Magnetic Properties Measurement System (MPMS3) with the Vibrating Sample Magnetometer. The films were measured from 2 to 300 K under applied fields from −7 to +7 T. The measured $MnCoN_2$ film was an approximately 5 × 5 mm piece of a combinatorial film grown on a Si substrate. It was approximately 600 nm thick with composition Mn/(Co + Mn) = 0.5 ± 0.01 as measured by XRF. To isolate the signal of the film, a bare substrate was also measured and subtracted.

C. Calculations

To calculate the total energy, we employed the strongly constrained and appropriately normed (SCAN) meta-GGA functional [61] in density functional theory (DFT) with the projected augmented wave (PAW) method as implemented in the Vienna *ab-initio* Simulation Package (VASP) [62–64]. We used on-site Coulomb interaction [65] of $U = 2$ eV for both the Mn-d and Co-d orbitals as determined in [66] for the SCAN functional. Calculations were spin-polarized to account for the expected magnetic moment of Mn and Co. The soft "N_s" PAW potential was employed to allow for a reduced energy cutoff of 380 eV [67]. Further, the final energies were obtained with a Brillouin zone sampling of 4000 k-points per reciprocal atom, and the atomic forces were relaxed to below 0.01 meV/Å during the full structural relaxation.

[1] X.-J. Chen *et al.*, Hard superconducting nitrides, Proc. Natl. Acad. Sci. USA **102**, 3198 (2005).

[2] M. Dasog, Transition metal nitrides are heating up the field of plasmonics, Chem. Mater. **34**, 4249 (2022).

[3] K. R. Talley, C. L. Perkins, D. R. Diercks, G. L. Brennecka, and A. Zakutayev, Synthesis of LaWN$_3$ nitride perovskite with polar symmetry, Science **374**, 1488 (2021).

[4] J.-P. Wang, Environment-friendly bulk Fe$_{16}$N$_2$ permanent magnet: Review and prospective, J. Magn. Magn. Mater. **497**, 165962 (2020).

[5] Y. Hinuma *et al.*, Discovery of earth-abundant nitride semiconductors by computational screening and high-pressure synthesis, Nat. Commun. **7**, 11962 (2016).

[6] H. K. Singh *et al.*, High-throughput screening of magnetic antiperovskites, Chem. Mater. **30**, 6983 (2018).

[7] R. Khaledialidusti, M. Khazaei, S. Khazaei, and K. Ohno, High-throughput computational discovery of ternary-layered MAX phases and prediction of their exfoliation for formation of 2D MXenes, Nanoscale **13**, 7294 (2021).

[8] W. Sun *et al.*, A map of the inorganic ternary metal nitrides, Nat. Mater. **18**, 732 (2019).

[9] G. Hautier, C. Fischer, V. Ehrlacher, A. Jain, and G. Ceder, Data mined ionic substitutions for the discovery of new compounds, Inorg. Chem. **50**, 656 (2011).

[10] S. R. Bauers *et al.*, Ternary nitride semiconductors in the rocksalt crystal structure, Proc. Natl. Acad. Sci. USA **116**, 14829 (2019).

[11] S. R. Bauers *et al.*, Composition, structure, and semiconducting properties of Mg$_x$Zr$_{2-x}$N$_2$ thin films, Jpn. J. Appl. Phys. **58**, SC1015 (2019).

[12] A. L. Greenaway *et al.*, Combinatorial synthesis of magnesium tin nitride semiconductors, J. Am. Chem. Soc. **142**, 8421 (2020).

[13] R. Woods-Robinson *et al.*, The role of disorder in the synthesis of metastable ternary nitrides, Phys. Rev. Mater. **6**, 043804 (2022).

[14] E. Arca *et al.*, Zn$_2$SbN$_3$: Growth and characterization of a metastable photoactive semiconductor, Mater. Horiz. **6**, 1669.

[15] C. L. Rom *et al.*, Combinatorial synthesis of cation-disordered manganese tin nitride MnSNn$_2$ thin films with magnetic and semiconducting properties, Chem. Mater. **35**, 2936 (2023).

[16] S. Zhuk *et al.*, Combinatorial reactive sputtering with auger parameter analysis enables synthesis of wurtzite Zn$_2$TaN$_3$, Chem. Mater. **35**, 7069 (2023).

[17] S. Zhuk and S. Siol, Chemical state analysis of reactively sputtered zinc vanadium nitride: The Auger parameter as a tool in materials design, Appl. Surf. Sci. **601**, 154172 (2022).

[18] A. Jain *et al.*, Commentary: The Materials Project: A materials genome approach to accelerating materials innovation, APL Mater. **1**, 011002 (2013).

[19] K. Suzuki *et al.*, Crystal structure and magnetic properties of the compound MnN, J. Alloys Compd. **306**, 66 (2000).

[20] A. Janotti, S.-H. Wei, and L. Bellaiche, Electronic and magnetic properties of MnN versus MnAs, Appl. Phys. Lett. **82**, 766 (2003).

[21] L. Li, K. Bao, X. Zhao, and T. Cui, Bonding properties of manganese nitrides at high pressure and the discovery of MnN4 with planar N4 rings, J. Phys. Chem. C **125**, 24605 (2021).

[22] X. Zheng *et al.*, Pressure-induced first-order antiferromagnetic to ferromagnetic transition in MnN, J. Alloys Compd. **935**, 168120 (2023).

[23] A. Zakutayev, S. R. Bauers, and S. Lany, Experimental synthesis of theoretically predicted multivalent ternary nitride materials, Chem. Mater. **34**, 1418 (2022).

[24] O. Schmitz-Dumont and N. Kron, Bei thermischem Abbau von Kobalt (III)-amid entstehende Kobaltnitride, Angew. Chem. **67**, 231 (1955).

[25] T. B. Joyner and F. H. Verhoek, Products of the thermal decomposition of some cobalt ammine azides, J. Am. Chem. Soc. **83**, 1069 (1961).

[26] K. Suzuki, T. Kaneko, H. Yoshida, H. Morita, and H. Fujimori, Crystal structure and magnetic properties of the compound CoN, J. Alloys Compd. **224**, 232 (1995).

[27] P. Lukashev and W. R. L. Lambrecht, First-principles study of the preference for zinc-blende or rocksalt structures in FeN and CoN, Phys. Rev. B **70**, 245205 (2004).

[28] C. Oses, C. Toher, and S. Curtarolo, High-entropy ceramics, Nat. Rev. Mater. **5**, 295 (2020).

[29] R. J. Clément, Z. Lun, and G. Ceder, Cation-disordered rocksalt transition metal oxides and oxyfluorides for high energy lithium-ion cathodes, Energy Environ. Sci. **13**, 345 (2020).

[30] M. Jankousky, H. Chen, A. Novick, and V. Stevanović, All "roads" lead to rocksalt structure, J. Am. Chem. Soc. **146**, 23004 (2024).

[31] See Supplemental Material at http://link.aps.org/supplemental/10.1103/PhysRevMaterials.8.104411 for additional figures.

[32] W. Lengauer, Nitrides: Transition Metal Solid-State Chemistry, in *Encyclopedia of Inorganic and Bioinorganic Chemistry* 1–24 (Wiley, Hoboken, New Jersey, 2015).

[33] R. Yuan *et al.*, Coral-like Cu-Co-mixed oxide for stable electroproperties of glucose determination, Electrochim. Acta **273**, 502 (2018).

[34] J. Yang *et al.*, Co_3O_4 nanocrystals derived from a zeolitic imidazolate framework on Ni foam as high-performance supercapacitor electrode material, RSC Adv. **6**, 61803 (2016).

[35] T. Choudhury, S. O. Saied, J. L. Sullivan, and A. M. Abbot, Reduction of oxides of iron, cobalt, titanium and niobium by low-energy ion bombardment, J. Phys. Appl. Phys. **22**, 1185 (1989).

[36] J. Masa *et al.*, Amorphous cobalt boride (Co_2B) as a highly efficient nonprecious catalyst for electrochemical water splitting: Oxygen and hydrogen evolution, Adv. Energy Mater. **6**, 1502313 (2016).

[37] R. Zeng *et al.*, Nonprecious transition metal nitrides as efficient oxygen reduction electrocatalysts for alkaline fuel cells, Sci. Adv. **8**, eabj1584 (2022).

[38] K. Zhu, C. Jin, Z. Klencsár, A. S. Ganeshraja, and J. Wang, Cobalt-iron oxide, alloy and nitride: Synthesis, characterization and application in catalytic peroxymonosulfate activation for orange II degradation, Catalysts **7**, 138 (2017).

[39] D. Su *et al.*, CoO-Mo_2N hollow heterostructure for high-efficiency electrocatalytic hydrogen evolution reaction, NPG Asia Mater. **11**, 1 (2019).

[40] S. C. Petitto and M. A. Langell, Surface composition and structure of Co_3O_4(110) and the effect of impurity segregation, J. Vac. Sci. Technol. A **22**, 1690 (2004).

[41] J. L. Mendes *et al.*, Interfacial states, energetics, and atmospheric stability of large-grain antifluorite Cs_2TiBr_6, J. Phys. Chem. C **124**, 24289 (2020).

[42] R. Sereika *et al.*, Prolonged mixed phase induced by high pressure in MnRuP, Phys. Rev. B **97**, 214103 (2018).

[43] K.-W. Nam, M. G. Kim, and K.-B. Kim, In Situ Mn K-edge x-ray absorption spectroscopy studies of electrodeposited manganese oxide films for electrochemical capacitors, J. Phys. Chem. C **111**, 749 (2007).

[44] F. Farges, Ab initio and experimental pre-edge investigations of the Mn *K*-edge XANES in oxide-type materials, Phys. Rev. B **71**, 155109 (2005).

[45] H. Su *et al.*, Hierarchical Mn_2O_3 hollow microspheres as anode material of lithium ion battery and its conversion reaction mechanism investigated by XANES, ACS Appl. Mater. Interfaces **7**, 8488 (2015).

[46] J. G. Moya-Cancino *et al.*, Elucidating the K-edge x-ray absorption near-edge structure of cobalt carbide, ChemCatChem **11**, 3042 (2019).

[47] K. R. Talley *et al.*, Synthesis of lanthanum tungsten oxynitride perovskite thin films, Adv. Electron. Mater. **5**, 1900214 (2019).

[48] V. Celorrio *et al.*, Relationship between Mn oxidation state changes and oxygen reduction activity in (La,Ca)MnO$_3$ as probed by In Situ XAS and XES, ACS Catal. **11**, 6431 (2021).

[49] E. P. Jahrman, K. L. S. Masias, T. C. Peck, and C. A. Roberts, X-ray absorption fine structure characterization of a multicomponent spinel catalyst, X-Ray Spectrom. **52**, 90 (2023).

[50] R. D. Shannon, Revised effective ionic radii and systematic studies of interatomic distances in halides and chalcogenides, Acta Crystallogr. A **32**, 751 (1976).

[51] M. Abuín, A. Serrano, J. Chaboy, M. A. García, and N. Carmona, XAS study of Mn, Fe and Cu as indicators of historical glass decay, J. Anal. At. Spectrom. **28**, 1118 (2013).

[52] W. J. Takei, G. Shirane, and B. C. Frazer, Magnetic structure of Mn_4N, Phys. Rev. **119**, 122 (1960).

[53] M. Tabuchi, M. Takahashi, and F. Kanamaru, Relation between the magnetic transition temperature and magnetic moment for manganese nitrides $MnN\gamma$ ($O < \gamma < 1$), J. Alloys Compd. **210**, 143 (1994).

[54] B. Balasubramanian *et al.*, Magnetism of new metastable cobalt-nitride compounds, Nanoscale **10**, 13011 (2018).

[55] M. Sato *et al.*, Dilution effect on magnetic properties of Co_3O_4 nanocrystals, J. Appl. Phys. **88**, 2771 (2000).

[56] K. R. Talley *et al.*, COMBIgor: Data-analysis package for combinatorial materials science, ACS Comb. Sci. **21**, 537 (2019).

[57] A. Zakutayev *et al.*, An open experimental database for exploring inorganic materials, Sci. Data **5**, 1 (2018).

[58] K. R. Talley *et al.*, Research data infrastructure for high-throughput experimental materials science, Patterns **2**, 100373 (2021).

[59] N. P. Barradas *et al.*, Summary of IAEA intercomparison of IBA software, Nucl. Instrum. Methods Phys. Res. Sect. B Beam Interact. Mater. At. **266**, 1338 (2008).

[60] B. Ravel and M. Newville, ATHENA, ARTEMIS, HEPHAESTUS: Data analysis for X-ray absorption spectroscopy using IFEFFIT, J. Synch. Radiat. **12**, 537 (2005).

[61] J. Sun, A. Ruzsinszky, and J. P. Perdew, Strongly constrained and appropriately normed semilocal density functional, Phys. Rev. Lett. **115**, 036402 (2015).

[62] P. E. Blöchl, Projector augmented-wave method, Phys. Rev. B **50**, 17953 (1994).

[63] G. Kresse and D. Joubert, From ultrasoft pseudopotentials to the projector augmented-wave method, Phys. Rev. B **59**, 1758 (1999).

[64] G. Kresse and J. Furthmüller, Efficient iterative schemes for ab initio total-energy calculations using a plane-wave basis set, Phys. Rev. B **54**, 11169 (1996).

[65] S. L. Dudarev, G. A. Botton, S. Y. Savrasov, C. J. Humphreys, and A. P. Sutton, Electron-energy-loss spectra and the structural stability of nickel oxide: An LSDA+U study, Phys. Rev. B **57**, 1505 (1998).

[66] A. Goyal, M. D. Sanders, R. P. O'Hayre, and S. Lany, Predicting thermochemical equilibria with interacting defects: $Sr_{1-x}Ce_xO_{3-d}$ alloys for water splitting, PRX Energy **3**, 013008 (2024).

[67] H. Peng *et al.*, Convergence of density and hybrid functional defect calculations for compound semiconductors, Phys. Rev. B **88**, 115201 (2013).